Journal of Materials Chemistry A

ROYAL SOCIETY OF CHEMISTRY

PAPER

View Article Online
View Journal | View Issue





Cite this: *J. Mater. Chem. A*, 2020, **8**, 592

# High-performance alcohol electrooxidation on $Pt_3Sn–SnO_2$ nanocatalysts synthesized through the transformation of Pt–Sn nanoparticles†

Liang Wang,[ab] Wei Wu,[ab] Zhao Lei,[ab] Tang Zeng,[ab] Yangyang Tan,[ab] Niancai Cheng *[ab] and Xueliang Sun*[c]

In this work, $Pt_3Sn–SnO_2$ supported on N-doped graphene ($Pt_3Sn–SnO_2$/NG) was synthesized through the *in situ* transformation of Pt–Sn/NG by annealing in an air atmosphere. The $Pt_3Sn–SnO_2$/NG catalyst, characterized by XRD, TEM and HRTEM, forms an ordered $Pt_3Sn$ intermetallic in which every $Pt_3Sn$ nanoparticle (NP) is in close contact with one or more $SnO_2$ NPs. The $Pt_3Sn–SnO_2$/NG catalyst shows outstanding performance towards the ethanol oxidation reaction (EOR) and methanol oxidation reaction (MOR). The mass activity for EOR on the $Pt_3Sn–SnO_2$/NG catalyst is 469 mA $mg_{Pt}^{-1}$ at 0.7 V, which is more than 10 times that of the commercial Pt/C catalyst (44 mA $mg_{Pt}^{-1}$). The $Pt_3Sn–SnO_2$/NG catalyst is found to have more than three times the stability of the commercial Pt/C. Our $Pt_3Sn–SnO_2$/NG catalyst also delivers increased activity and higher stability for MOR compared with the Pt/C catalyst. In addition, the $Pt_3Sn–SnO_2$/NG catalyst is observed to have a higher CO tolerance compared with Pt/C. The high activity and stability of the $Pt_3Sn–SnO_2$/NG catalyst can be attributed to the unique structure of $Pt_3Sn–SnO_2$, formed by the *in situ* transformation of Pt–Sn/NG, which induces the formation of a small-sized ordered $Pt_3Sn$ intermetallic that strongly interacts with $SnO_2$. The synergetic effect between the ordered $Pt_3Sn$ and $SnO_2$ enhances the activity towards EOR and MOR through the Sn in both $Pt_3Sn$ and $SnO_2$, which facilitates the removal of $CO_{ads}$ on the adjacent Pt active sites at low potentials by providing $OH_{ads}$ species; it also improves stability because of the strong $Pt_3Sn–SnO_2$ interactions.

Received 2nd October 2019
Accepted 29th November 2019

DOI: 10.1039/c9ta10886f

rsc.li/materials-a

## Introduction

Direct alcohol fuel cells (DAFCs) including direct ethanol fuel cells (DEFCs) and direct methanol fuel cells (DMFCs) are regarded as promising energy conversion devices for portable electronic devices because of their high power densities, low operating temperatures, low emissions, and safety for storage and transportation.[1–4] However, the commercialization of DAFCs has been hindered by their low activities and the instabilities of the anode electrocatalysts which originate from the intrinsically sluggish kinetics of the ethanol oxidation reaction (EOR) and methanol oxidation reaction (MOR).[5–7] Pt nanoparticles (NPs) deposited on carbon supports have been widely used to facilitate alcohol oxidation in DAFCs.[8–11] However, the Pt catalysts are easily poisoned by the surface adsorbed intermediates such as CO produced during decomposition of methanol and ethanol, leading to the loss of Pt catalytic activity.[12] Moreover, the weak interactions between carbon black and Pt NPs also lead to a degradation in Pt catalytic activity due to particle migration and agglomeration caused by the easy migration of the particles on the carbon supports during the long-term operation of DAFCs.[13–15]

Recently, much more effort has been made to increase the Pt utilization and decrease the Pt usage through the enhanced electrocatalytic performance towards MOR and EOR that can be realized by alloying platinum (Pt) with other transition metals (M).[16] The different kinds of Pt–M alloy electrocatalysts, such as Pt–Sn,[17–19] Pt–Ru[4,20] and Pt–Co,[21,22] have been reported to achieve enhanced MOR and EOR activity in comparison with their counterpart pure Pt catalysts, due to the bifunctional and/or ligand effects between the two metals. Unfortunately, the electrochemical performances of most of these Pt-based alloy electrocatalysts still suffer from degradation during long-term operation, which is mainly caused by the dissolution of the non-noble metals in the harsh environments of the DAFCs. Recently, much attention has been focused on the development of structurally-ordered Pt-based intermetallic catalysts to further improve activity and stability by alleviating the metal dissolution of non-noble metals due to the increased strength of

[a]College of Materials Science and Engineering, Fuzhou University, Fuzhou, 350108, China. E-mail: niancaicheng@fzu.edu.cn

[b]Key Laboratory of Eco-materials Advanced Technology, Fuzhou University, Fuzhou, 350108, China

[c]Department of Mechanical and Materials Engineering, The University of Western Ontario, London, ON N6A 5B9, Canada. E-mail: xsun@eng.uwo.ca

† Electronic supplementary information (ESI) available. See DOI: 10.1039/c9ta10886f

Pt–M bonds and Pt–M interactions.[23–27] Among the various Pt-based intermetallic electrocatalysts, $Pt_3Sn$ intermetallic NPs have attracted extensive attention because they exhibit high activity and stability towards MOR and EOR along with high tolerance to CO poisoning in acidic media.[28–31]

The development of a synergetic effect through the strong interactions of Pt and metal oxides on carbon supports is another efficient strategy for improving the Pt activity and durability for MOR and EOR.[32–34] The role of the metal oxides is not only to generate strong interactions with Pt to alter the electronic properties of Pt and so increase the electrocatalytic performance, but also to facilitate the removal of $CO_{ads}$ on the adjacent Pt active sites at low potentials by providing $OH_{ads}$ species.[12] Among various metal oxide materials, $SnO_2$ has been widely employed for enhancing MOR and EOR activity due to its low cost, generation of OH species at low potentials, and formation of strong interactions with Pt.[1] For instance, Li *et al.*[35] prepared a Pt–$SnO_2$/graphene composite with strong Pt–$SnO_2$ interactions, resulting in higher electrocatalytic activity and durability for MOR than that of Pt/graphene. Compared with Pt/NCNC (nitrogen-doped carbon nanocages), Pt-0.5$SnO_x$/NCNC displayed a better EOR performance in acidic medium because OH species generated on the $SnO_x$ sites were beneficial for the oxidative removal of CO species adsorbed at Pt sites.[36] Therefore, it is crucial to precisely control the contact between the Pt NPs and metal oxides on a carbon support to form Pt–metal oxide interfaces, thus leading to strong interactions between Pt and the metal oxides and high electrocatalytic activity. However, the precise control of the contact between the metal and oxide is still a challenge to achieve through traditional methods in which the metal oxides are deposited on Pt NPs supported on carbon supports, or the Pt NPs are deposited on metal oxides supported on carbon supports.

In this work, we propose a facile strategy to prepare $Pt_3Sn$–$SnO_2$ supported on N-doped graphene (NG) by the *in situ* transformation of Pt–Sn/NG. The *in situ* transformation of Pt–Sn/NG to $Pt_3Sn$–$SnO_2$/NG not only induces the formation of ordered $Pt_3Sn$ NPs and $SnO_2$, but also precisely controls the contact between $Pt_3Sn$ and $SnO_2$ to generate strong $Pt_3Sn$–$SnO_2$ interactions. The $Pt_3Sn$–$SnO_2$/NG catalyst displayed excellent electrocatalytic activity and stability towards MOR and EOR. Furthermore, the $Pt_3Sn$–$SnO_2$/NG catalyst showed high CO tolerance. These results provide important clues for the rational design of highly active and stable Pt-based ordered intermetallic electrocatalysts for fuel cell applications.

## Results and discussion

Scheme 1 illustrates the synthesis process for the $Pt_3Sn$–$SnO_2$/NG electrocatalyst by the *in situ* transformation of Pt–Sn/NG. The Pt–Sn alloy NPs were firstly synthesized and then they were anchored on the surface of NG. Through annealing at 300 °C in an air atmosphere for 1 h, the Pt–Sn alloy NPs transformed into two different NPs of $Pt_3Sn$ and $SnO_2$ which were in close contact on the surface of NG. The morphological structures of the as-prepared catalysts were characterized by transmission electron microscopy (TEM). Fig. S1† displays the

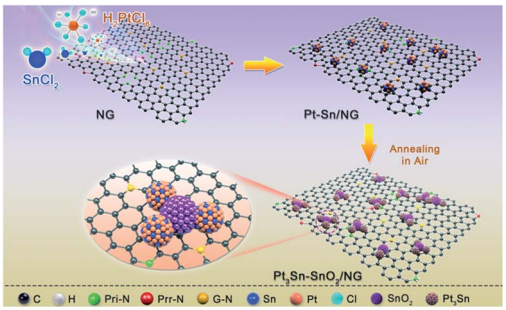


Scheme 1 Schematic illustration of the strategy for the synthesis of $Pt_3Sn$–$SnO_2$ on N-doped graphene.

TEM images of the Pt–Sn alloy NPs uniformly dispersed on the surface of NG with average sizes of *ca.* 3.4 nm. It is obvious that the density of the NPs on the surface of NG increased after the annealing treatment (Fig. 1a), mainly due to the transformation of the Pt–Sn alloy NPs into $Pt_3Sn$ and $SnO_2$ NPs. The high-resolution TEM (HRTEM) image (Fig. 1b) shows crystalline fringes with interplanar spacings of 0.231 nm and 0.200 nm, corresponding to the (111) and (200) lattice spacings of the face centered cubic (fcc) structurally-ordered $Pt_3Sn$ NPs. The interplanar spacings of 0.237 nm and 0.335 nm derive from the (200) and (110) lattice spacings of the $SnO_2$, indicating the formation of $SnO_2$ NPs during the Pt–Sn/NG synthesis. More importantly, the HRTEM image of the $Pt_3Sn$–$SnO_2$/NG catalyst indicates that every $Pt_3Sn$ NP is in close contact with one or more $SnO_2$ NPs rather than being in separated depositions of $Pt_3Sn$ NPs and $SnO_2$ NPs on the surface of the NG. This suggests that the *in situ* transformation of Pt–Sn/NG is an effective strategy for precisely controlling the contact between $Pt_3Sn$ and $SnO_2$. This precisely

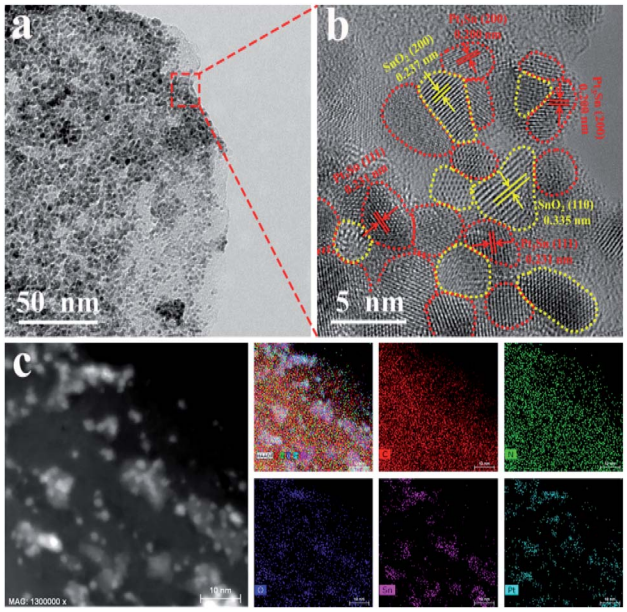


Fig. 1 (a) TEM and (b) HRTEM images of the $Pt_3Sn$–$SnO_2$/NG catalyst. (c) STEM image of the $Pt_3Sn$–$SnO_2$/NG catalyst and the corresponding elemental mappings of C, N, O, Sn and Pt.

controlled contact between $Pt_3Sn$ and $SnO_2$ is beneficial for enhancing the Pt performance for the oxidation of alcohol because it ensures strong interactions between the metal and metal oxides and it provides $OH_{ads}$ species.[37,38] Elemental mapping (Fig. 1c) shows that Pt, Sn, N and O are uniformly distributed in the $Pt_3Sn$–$SnO_2$/NG catalyst. The atomic ratio of Pt/Sn in the $Pt_3Sn$–$SnO_2$/NG catalyst was estimated to be about 3 : 1 based on inductively coupled plasma mass spectrometry (ICP); this is in good agreement with the formation of $Pt_3Sn$ NPs on NG as observed in the TEM measurements. Furthermore, the average size of the $Pt_3Sn$ NPs in the $Pt_3Sn$–$SnO_2$/NG catalyst is about 3.2 nm, which is smaller than that of the ordered $Pt_3Sn$-anchored NG prepared by direct annealing of a disordered $Pt_3Sn$ alloy on NG in an atmosphere of 10% $H_2$/90% $N_2$ (Fig. S2†). The finding suggests that the *in situ* transformation method can effectively control the size of the $Pt_3Sn$ NPs.

The structures of the $Pt_3Sn$–$SnO_2$/NG and Pt–Sn/NG catalysts were further characterized by X-ray diffraction (XRD). As shown in Fig. 2a, the Pt–Sn/NG catalyst shows diffraction peaks located at 39.3°, 45.9°, and 66.8°, corresponding to the Pt (111), (200), and (220) planes, which indicate a typical fcc structure for Pt. These peaks in the Pt–Sn/NG catalyst are shifted to lower diffraction angles in comparison with the peaks in a commercial Pt/C catalyst, as a result of the formation of the Pt–Sn alloy NPs on NG.[39] In addition, the broad diffraction peak centered at about 26° can be ascribed to the graphite structure (002) of NG. Compared with the Pt–Sn/NG catalyst, the diffraction peaks in the $Pt_3Sn$/NG catalyst are negatively shifted, suggesting the formation of $Pt_3Sn$ NPs after the direct annealing treatment of the disordered $Pt_3Sn$/NG catalyst. The XRD pattern of the $Pt_3Sn$–$SnO_2$/NG catalyst not only indicates the formation of $Pt_3Sn$ NPs through the broader diffraction peaks in comparison with those of the $Pt_3Sn$/NG catalyst, but also confirms the formation of $SnO_2$ NPs on NG after annealing the Pt–Sn alloy NPs at 300 °C in air; this is also consistent with the result of the TEM analysis. The Pt loadings on the $Pt_3Sn$–$SnO_2$/NG, Pt–Sn/NG and $Pt_3Sn$/NG catalysts were 12.2 wt%, 14.3 wt% and 14.9 wt%, respectively according to the ICP analysis. X-ray photoelectron spectroscopy (XPS) was carried out to study the surface structures and compositions of the different catalysts, as shown in Fig. S3† and 2b–d. The XPS spectra of the Pt 4f region for $Pt_3Sn$/NG (Fig. 2b) can be deconvoluted into two peaks corresponding to metallic Pt(0) and Pt(II) species located at 71.45/74.79 and 72.74/76.02 eV, respectively. For the $Pt_3Sn$–$SnO_2$/NG catalyst (Fig. 2b), the binding energies located at 71.55/74.79, 72.65/76.02, and 73.83/77.97 eV can be attributed to the $4f_{7/2}/4f_{5/2}$ peaks of Pt(0), Pt(II) and Pt(IV) species, respectively. The Pt 4f binding energies for various catalysts are listed in Table S1†. Table S1† clearly indicates that the Pt 4f binding energies for the $Pt_3Sn$–$SnO_2$/NG sample are negatively shifted in comparison with those of the Pt/C catalysts, which can be attributed to the increased Pt–Pt distances and the tuning of the Pt electronic structure caused by the ordered incorporation of Sn into the Pt lattices.[39] The downshift of Pt 4f in $Pt_3Sn$–$SnO_2$/NG may effectively lower its CO affinity and so inhibit CO adsorption on the Pt surface, leading to the increased activity of the catalyst for MOR and EOR.[40,41] Fig. 2c shows that the Pt–Sn/NG has binding energies at 485.56/494.09 and 487.08/495.5 eV, corresponding to Sn(0) and Sn(II/IV) species, respectively, due to the close binding energies between Sn(II) and Sn(IV).[42] The Sn 3d binding energies for various catalysts are summarized in Table S2†. Compared with the Pt–Sn/NG catalyst, the content of the Sn(0) species in the $Pt_3Sn$/NG catalyst is significantly increased while the content of the Sn(II/IV) species is decreased, arising from the ordered $Pt_3Sn$ intermetallic. It is obvious that the $Pt_3Sn$–$SnO_2$/NG catalyst shows a lower content of Sn(0) species and a higher content of Sn(II/IV) species in comparison with the $Pt_3Sn$/NG catalyst, which can mainly be attributed to the formation of $Pt_3Sn$–$SnO_2$ on NG. Fig. 2d shows that the annealing treatment at 300 °C in air did not significantly change the content of the different N doping configurations in NG.

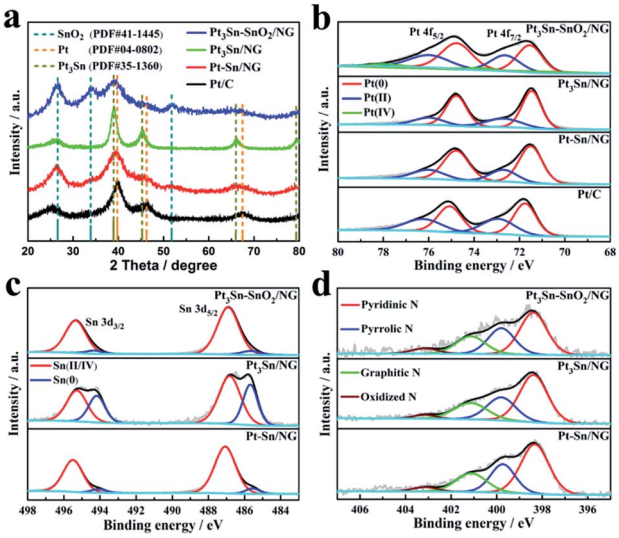


Fig. 2 (a) XRD patterns of the $Pt_3Sn$–$SnO_2$/NG, Pt–Sn/NG, $Pt_3Sn$/NG and Pt/C catalysts. (b) High-resolution Pt 4f spectra of the $Pt_3Sn$–$SnO_2$/NG, Pt–Sn/NG, $Pt_3Sn$/NG and Pt/C catalysts. High-resolution (c) Sn 3d and (d) N 1s spectra of the $Pt_3Sn$–$SnO_2$/NG, Pt–Sn/NG and $Pt_3Sn$/NG catalysts.

Tolerance to poisoning is crucial for maintaining Pt activity for MOR and EOR in DAFCs. CO stripping tests were first applied to evaluate the capability of various catalysts for CO oxidation (Fig. 3). The onset potentials for CO oxidation on $Pt_3Sn$–$SnO_2$/NG, $Pt_3Sn$/NG, Pt–Sn/NG and Pt/C catalysts are about 0.33 V, 0.38 V, 0.43 V and 0.83 V, respectively. In comparison with Pt/C, the lower onset potential of $Pt_3Sn$/NG (0.38 V) can be attributed to the bifunctional and/or ligand effects due to the incorporation of Sn into the Pt lattice, facilitating CO oxidation at relatively low potentials. The reduction by 50 mV of the onset potential for CO oxidation on the $Pt_3Sn$–$SnO_2$/NG catalyst in comparison with that of the $Pt_3Sn$/NG catalyst is mainly due to the synergetic effect between $Pt_3Sn$ and $SnO_2$, resulting in the occurrence of CO oxidation at lower potentials. The Pt/C catalyst shows only one CO oxidation peak at *ca.* 0.89 V while the other catalysts display three peaks for CO oxidation at lower potentials. The multi-peaks for CO oxidation can be attributed to the presence of multi-active sites for CO oxidation. The peak potentials for the $Pt_3Sn$–$SnO_2$/NG catalyst

 

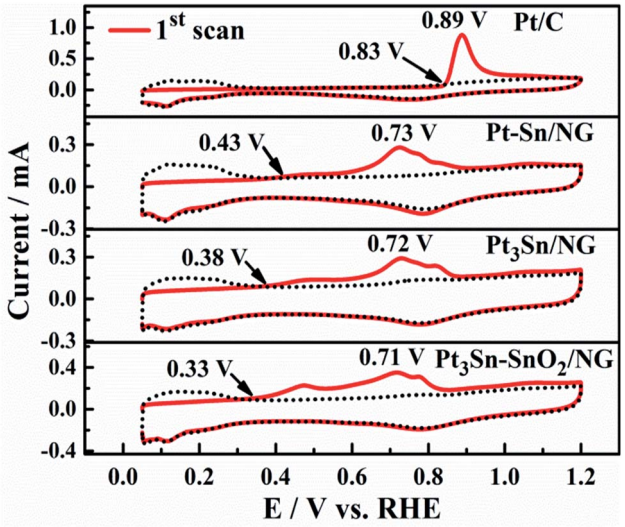


Fig. 3 CO stripping patterns recorded on $Pt_3Sn$–$SnO_2$/NG, Pt–Sn/NG, $Pt_3Sn$/NG and Pt/C in 0.5 M $H_2SO_4$.

are at about 0.47 V, 0.71 V and 0.78 V, which are lower than the corresponding peak potentials for the $Pt_3Sn$/NG catalyst (0.49 V, 0.72 V and 0.82 V). This finding further suggests that the synergetic effect between $Pt_3Sn$ and $SnO_2$ can facilitate CO oxidation. The electrochemically active surface area (ECSA) of the as-prepared samples was calculated from the oxidation of a monolayer of CO and are summarized in Table S3†.[43]

Cyclic voltammograms (CVs) as shown in Fig. 4a obviously demonstrate that there are no well-defined adsorption/desorption peaks for $Pt_3Sn$/NG and $Pt_3Sn$–$SnO_2$/NG because the insertion of Sn into the Pt lattice depresses hydrogen regions.[39] As shown in Fig. 4b and S4,† it is obvious that the $Pt_3Sn$–$SnO_2$/NG catalyst has a higher electrocatalytic activity

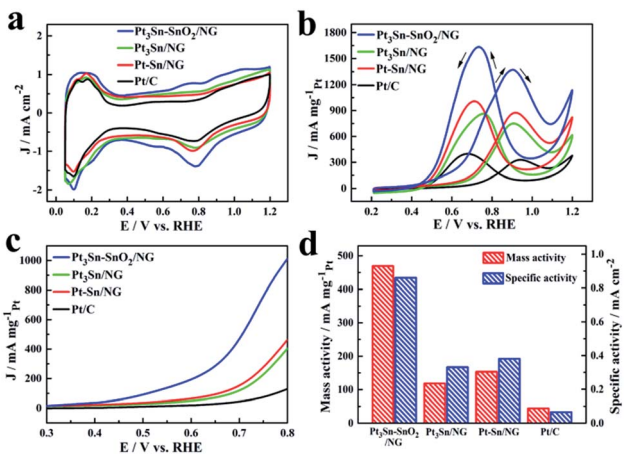


Fig. 4 Catalytic activity for EOR. (a) CV curves of different catalysts in 0.5 M $H_2SO_4$ solution with a sweep rate of 50 mV $s^{-1}$. (b) CV curves of different catalysts in 0.5 M $H_2SO_4$ + 1 M $CH_3CH_2OH$ solution with a sweep rate of 50 mV $s^{-1}$. (c) Linear sweep voltammograms of different catalysts in 0.5 M $H_2SO_4$ + 1 M $CH_3CH_2OH$ solution with a sweep rate of 50 mV $s^{-1}$. (d) The masses and specific activities of different catalysts at 0.7 V in 0.5 M $H_2SO_4$ + 1 M $CH_3CH_2OH$ solution.

towards EOR than that of the Pt–Sn/NG, $Pt_3Sn$/NG and Pt/C catalysts. The $Pt_3Sn$–$SnO_2$/NG catalyst achieved the lowest onset potential of 0.31 V as shown in Fig. 4c, which was lower than those of Pt–Sn/NG (0.44 V), $Pt_3Sn$/NG (0.39 V) and Pt/C (0.62 V), indicating that the $Pt_3Sn$–$SnO_2$/NG catalyst more easily catalyzes EOR. The $Pt_3Sn$–$SnO_2$/NG catalyst shows the highest specific activity and mass activity towards EOR over the full potential range (Fig. S5†). The specific activity (Fig. 4d) of the $Pt_3Sn$–$SnO_2$/NG catalyst is 0.86 mA $cm^{-2}$ at 0.7 V, higher than that of the other catalysts. More importantly, the mass activity for the $Pt_3Sn$–$SnO_2$/NG catalyst is 469 mA $mg_{Pt}^{-1}$ at 0.7 V, which is 3.06, 3.97 and 10.65 times higher than those of Pt–Sn/NG (153 mA $mg_{Pt}^{-1}$), $Pt_3Sn$/NG (118 mA $mg_{Pt}^{-1}$) and Pt/C (44 mA $mg_{Pt}^{-1}$), respectively. The peak current density of EOR for the $Pt_3Sn$–$SnO_2$/NG catalyst (Fig. S6†) is higher than those of most reported catalysts, as shown in Table S4†. These findings indicate that the $Pt_3Sn$–$SnO_2$/NG catalyst possesses both a low onset potential and a high activity towards EOR, resulting from the synergetic effect between $Pt_3Sn$ and $SnO_2$. In addition, the annealing temperature of Pt–Sn/NG in air affects the EOR activity as shown in Fig. S7.† Fig. S7a† shows that the annealing of Pt–Sn/NG at 200 or 400 °C resulted in poor EOR activity in comparison with that of the catalyst annealed at 300 °C, which can be attributed to the different morphologies of the catalysts (Fig. S7b–f†). The annealing of Pt–Sn/NG at 200 °C does not form the unique structure in which one $Pt_3Sn$ NP is in close contact with one or more $SnO_2$ NPs, while the annealing of Pt–Sn/NG at 400 °C results in agglomeration of the NPs due to the partial oxidation of NG at 400 °C in air. Compared with Pt–Sn/NG, the lower mass activity of the $Pt_3Sn$/NG is likely due to its larger particle size (Fig. S2†).

Besides high catalytic activity, excellent stability is a key factor for the commercialization of DEFCs. The stability of the as-prepared catalysts towards EOR were studied by the chronoamperometric curves as shown in Fig. 5a. It is clearly observed that the current density for all catalysts gradually decreases with testing time. The $Pt_3Sn$–$SnO_2$/NG catalyst displays a much higher mass current density in comparison with those of the Pt–Sn/NG, $Pt_3Sn$/NG and Pt/C catalysts during the tests. The $Pt_3Sn$–$SnO_2$/NG catalyst still retains a mass activity of 202 mA $mg_{Pt}^{-1}$ at a voltage of 0.7 V after 3600 s (Fig. 5b), which is higher than those of Pt–Sn/NG (55 mA $mg_{Pt}^{-1}$), $Pt_3Sn$/NG (45 mA $mg_{Pt}^{-1}$) and Pt/C (17 mA $mg_{Pt}^{-1}$). We also evaluated the durability of each catalyst for EOR using accelerated durability tests (ADTs) in which 5000 cycles were performed between 0.05 and 1.2 V at a scan rate of 50 mV $s^{-1}$ in 0.5 M $H_2SO_4$ solution containing 1 M $CH_3CH_2OH$ (Fig. 5c and S8†). As shown in Fig. 5d, the $Pt_3Sn$–$SnO_2$/NG catalyst retains about 48% of its initial mass activity, whereas the $Pt_3Sn$/NG catalyst, which does not have interactions with $SnO_2$, decreases by about 64% of its initial mass activity. The $Pt_3Sn$–$SnO_2$/NG catalyst has more than 3 times the stability of the Pt/C catalyst which retains only about 15% of its initial mass activity in the same ADT conditions. After the ADT test, it was obvious that serious ripening or aggregation of the Pt NPs had occurred in the Pt/C catalyst; the Pt NPs increased in size from 3–5 to 8–25 nm (Fig. S9†). In contrast, the size of the $Pt_3Sn$ NPs in the

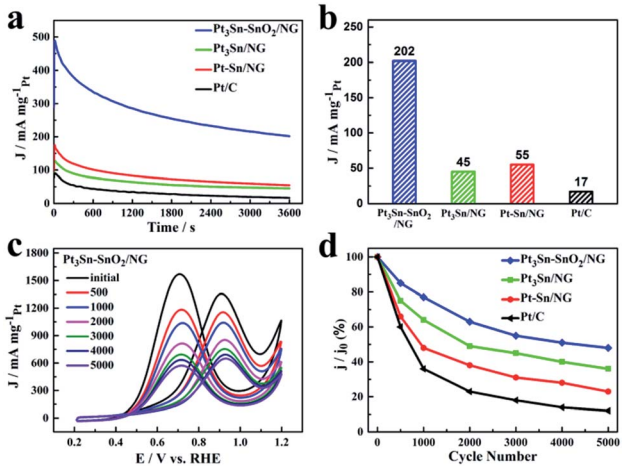


Fig. 5 Catalytic activity for EOR. (a) Chronoamperometric curves of different catalysts in $N_2$-saturated 0.5 M $H_2SO_4$ + 1 M $CH_3CH_2OH$ solution at a constant voltage of 0.7 V for 3600 s. (b) The current density for different catalysts obtained from (a). (c) Cyclic voltammograms of the $Pt_3Sn$–$SnO_2$/NG catalyst in $N_2$-saturated 0.5 M $H_2SO_4$ + 1 M $CH_3CH_2OH$ solution at a scan rate of 50 mV $s^{-1}$ during the durability tests. (d) Changes of peak current densities of EOR during the potential cycling of different catalysts.

$Pt_3Sn$–$SnO_2$/NG catalyst increased from 3–5 to only 4–8 nm and retained a narrow size distribution due to the high stability of the ordered $Pt_3Sn$ intermetallic due to the strong interactions with the contacted $SnO_2$ (Fig. 1 and S10†).

We also evaluated the performance of $Pt_3Sn$–$SnO_2$/NG as a catalyst for MOR. As expected, the $Pt_3Sn$–$SnO_2$/NG catalyst shows high activity and stability towards MOR. As shown in Fig. 6a and S11,† the $Pt_3Sn$–$SnO_2$/NG catalyst has a lower onset potential in comparison with those of Pt–Sn/NG, $Pt_3Sn$/NG and Pt/C. At 0.7 V, the mass activity towards MOR is 541 mA $mg_{Pt}^{-1}$ on the $Pt_3Sn$–$SnO_2$/NG catalyst, outperforming the Pt–Sn/NG (236 mA $mg_{Pt}^{-1}$), $Pt_3Sn$/NG (181 mA $mg_{Pt}^{-1}$) and Pt/C (109 mA $mg_{Pt}^{-1}$) catalysts (Fig. 6b). These results indicate that the MOR activity of the $Pt_3Sn$–$SnO_2$/NG catalyst is 2.29, 2.99 and 4.96 times higher than those of the Pt–Sn/NG, $Pt_3Sn$/NG and Pt/C catalysts, respectively. The $Pt_3Sn$–$SnO_2$/NG catalyst also shows the highest specific activity towards MOR (Fig. 6b, S12 and S13†). Compared with most reported catalysts, the $Pt_3Sn$–$SnO_2$/NG catalyst (Fig. S14†) shows higher MOR activity (Table S5†). After chronoamperometric measurements at a fixed potential of 0.7 V for 3600 s (Fig. 6c), the $Pt_3Sn$–$SnO_2$/NG catalyst still possesses 314 mA $mg_{Pt}^{-1}$ of mass activity, which is higher than those of Pt–Sn/NG (78 mA $mg_{Pt}^{-1}$), $Pt_3Sn$/NG (65 mA $mg_{Pt}^{-1}$) and Pt/C (30 mA $mg_{Pt}^{-1}$) (Fig. S15†). This finding suggests that the $Pt_3Sn$–$SnO_2$/NG catalyst has a higher stability than the other catalysts, which is also confirmed by the ADTs. After 5000 cycles, only 14% of the initial current density is observed for the Pt/C catalyst (Fig. 6d and S16†) while the $Pt_3Sn$–$SnO_2$/NG catalyst retains 46% of its initial current density. This finding demonstrates that the $Pt_3Sn$–$SnO_2$/NG catalyst is more stable for MOR than the Pt/C catalyst.

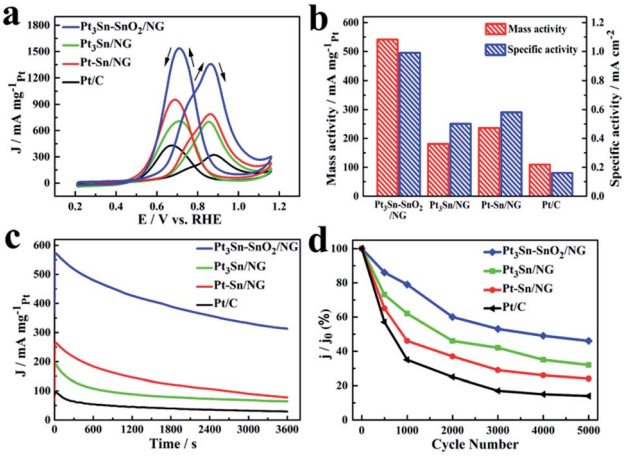


Fig. 6 Catalytic activity for MOR. (a) CV curves of different catalysts in 0.5 M $H_2SO_4$ + 1 M $CH_3OH$ solution with a sweep rate of 50 mV $s^{-1}$. (b) The masses and specific activities of different catalysts at 0.7 V in 0.5 M $H_2SO_4$ + 1 M $CH_3OH$ solution. (c) Chronoamperometric curves of different catalysts in $N_2$-saturated 0.5 M $H_2SO_4$ + 1 M $CH_3OH$ solution at a constant voltage of 0.7 V for 3600 s. (d) Changes of peak current densities of MOR during potential cycling of different catalysts.

The high activity and durability of the $Pt_3Sn$–$SnO_2$/NG catalyst towards EOR and MOR can be ascribed to the synergetic effect between $Pt_3Sn$ and $SnO_2$ and the ordered crystal structure of the $Pt_3Sn$ NPs. The incorporation of Sn into the Pt lattice improves the activity and stability of the catalyst towards EOR and MOR through the bifunctional and/or ligand effects. The Sn in $Pt_3Sn$ provides $OH_{ads}$ species for adjacent Pt by promoting water activation at a relatively low potential, facilitating the oxidation of the CO-like species intermediates produced during methanol and ethanol oxidation. In addition, the ordered crystal structure of $Pt_3Sn$ NPs increases the performance for MOR and EOR due to the increase in Pt–Pt distance and the modification of the Pt electronic structure, which effectively lowers the CO affinity and inhibits CO adsorption on Pt.[40,41] The fact that $SnO_2$ is in close contact with the $Pt_3Sn$ NPs enhances the MOR and EOR activity through the provision of $OH_{ads}$ species adsorbed on the surface of the $SnO_2$ and the alteration of the Pt electronic structure due to the strong interactions between $Pt_3Sn$ and $SnO_2$.[44] The synergetic effect between $Pt_3Sn$ and $SnO_2$ leads to enhanced MOR and EOR performances for the $Pt_3Sn$–$SnO_2$/NG catalyst in comparison to those for the $Pt_3Sn$/NG catalyst.

## Conclusions

In summary, we have developed a highly active and stable $Pt_3Sn$–$SnO_2$/NG catalyst through the *in situ* transformation of PtSn/NG by annealing in an air atmosphere. The $Pt_3Sn$–$SnO_2$/NG catalyst is observed to form an ordered $Pt_3Sn$ intermetallic on the surface of NG, in which each $Pt_3Sn$ NP is in close contact with one or more $SnO_2$ NPs. Compared with commercial Pt/C, the $Pt_3Sn$–$SnO_2$/NG catalyst possesses higher activity and stability towards EOR and MOR. In addition, the $Pt_3Sn$–$SnO_2$/NG catalyst is found to have better CO tolerance than Pt/C. The high activity and stability of the $Pt_3Sn$–$SnO_2$/NG catalyst is

 

attributed to the synergetic effect between the ordered $Pt_3Sn$ and $SnO_2$. The synergetic effect between the ordered $Pt_3Sn$ and $SnO_2$ enhances the activity towards EOR and MOR because the Sn in both $Pt_3Sn$ and $SnO_2$ facilitates the removal of $CO_{ads}$ on the adjacent Pt active sites at low potentials by providing OH species. Moreover, the stability of the catalyst is improved by the strong $Pt_3Sn$–$SnO_2$ interactions. The results of this work highlight a reliable strategy for the design of highly active and stable electrocatalysts for fuel cells through the synergetic effect of strong interactions between structurally-ordered Pt-based NPs and metal oxides on supports.

## Conflicts of interest

There are no conflicts to declare.

## Acknowledgements

This work was supported by the National Natural Science Foundation of China (Grant no. 21875039), a Minjiang Professorship (XRC-1677), Fujian Province's High Level Innovative and Entrepreneurial Talents (50012709), and the Open Project Program of the State Key Laboratory of Photocatalysis on Energy and Environment (Grant no. SKLPEE-201814), Fuzhou University.

## Notes and references

1 M. Mansor, S. N. Timmiati, K. L. Lim, W. Y. Wong, S. K. Kamarudin and N. H. Nazirah Kamarudin, *Int. J. Hydrogen Energy*, 2019, **44**, 14744–14769.
2 H. Liu, C. Song, L. Zhang, J. Zhang, H. Wang and D. P. Wilkinson, *J. Power Sources*, 2006, **155**, 95–110.
3 X. Zhao, M. Yin, L. Ma, L. Liang, C. P. Liu, J. H. Liao, T. H. Lu and W. Xing, *Energy Environ. Sci.*, 2011, **4**, 2736–2753.
4 L. Yang, J. J. Ge, C. P. Liu, G. L. Wang and W. Xing, *Curr. Opin. Electrochem.*, 2017, **4**, 83–88.
5 J. F. Chang, L. G. Feng, C. P. Liu and W. Xing, *Chemsuschem*, 2015, **8**, 3340–3347.
6 L. G. Feng, K. Li, J. F. Chang, C. P. Liu and W. Xing, *Nano Energy*, 2015, **15**, 462–469.
7 D. B. Huang, Q. Yuan, P. L. He, K. Wang and X. Wang, *Nanoscale*, 2016, **8**, 14705–14710.
8 B. W. Zhang, H. L. Yang, Y. X. Wang, S. X. Dou and H. K. Liu, *Adv. Eng. Mater.*, 2018, **8**, 1703597.
9 M. M. Li, Q. G. Jiang, M. M. Yan, Y. J. Wei, J. B. Zong, J. F. Zhang, Y. P. Wu and H. J. Huang, *ACS Sustainable Chem. Eng.*, 2018, **6**, 6644–6653.
10 X. Yang, J. Xue and L. Feng, *Chem. Commun.*, 2019, **55**, 11247–11250.
11 N. Tian, B.-A. Lu, X.-D. Yang, R. Huang, Y.-X. Jiang, Z.-Y. Zhou and S.-G. Sun, *Electrochem. Energy Rev.*, 2018, **1**, 54–83.
12 G. J. Chen, Z. F. Dai, L. Sun, L. Zhang, S. Liu, H. W. Bao, J. L. Bi, S. C. Yang and F. Ma, *J. Mater. Chem. A*, 2019, **7**, 6562–6571.
13 V. C. Anitha, R. Zazpe, M. Krbal, J. Yoo, H. Sopha, J. Prikryl, G. Cha, S. Slang, P. Schmuki and J. M. Macak, *J. Catal.*, 2018, **365**, 86–93.
14 N. Cheng, M. N. Banis, J. Liu, A. Riese, X. Li, R. Li, S. Ye, S. Knights and X. Sun, *Adv. Mater.*, 2015, **27**, 277–281.
15 N. C. Cheng, M. N. Banis, J. Liu, A. Riese, S. C. Mu, R. Y. Li, T. K. Sham and X. L. Sun, *Energy Environ. Sci.*, 2015, **8**, 1450–1455.
16 X. L. Tian, L. J. Wang, P. L. Deng, Y. Chen and B. Y. Xia, *J. Energy Chem.*, 2017, **26**, 1067–1076.
17 L. Li, H. Liu, C. Qin, Z. Liang, A. Scida, S. Yue, X. Tong, R. R. Adzic and S. S. Wong, *ACS Appl. Nano Mater.*, 2018, **1**, 1104–1115.
18 P. Song, X. Cui, Q. Shao, Y. Feng, X. Zhu and X. Huang, *J. Mater. Chem. A*, 2017, **5**, 24626–24630.
19 E. Leal da Silva, A. Cuña, M. Rita Ortega Vega, C. Radtke, G. Machado, N. Tancredi and C. de Fraga Malfatti, *Appl. Catal., B*, 2016, **193**, 170–179.
20 S. C. Zignani, V. Baglio, D. Sebastián, S. Siracusano and A. S. Aricò, *Electrochim. Acta*, 2016, **191**, 183–191.
21 R. Ahmadi, M. K. Amini and J. C. Bennett, *J. Catal.*, 2012, **292**, 81–89.
22 C. Xu, Y. Su, L. Tan, Z. Liu, J. Zhang, S. Chen and S. P. Jiang, *Electrochim. Acta*, 2009, **54**, 6322–6326.
23 T. Wang, J. Liang, Z. Zhao, S. Li, G. Lu, Z. Xia, C. Wang, J. Luo, J. Han, C. Ma, Y. Huang and Q. Li, *Adv. Eng. Mater.*, 2019, **9**, 1803771.
24 K. Jiang, P. Wang, S. Guo, X. Zhang, X. Shen, G. Lu, D. Su and X. Huang, *Angew. Chem.*, 2016, **55**, 9030–9035.
25 Q. Li, L. Wu, G. Wu, D. Su, H. Lv, S. Zhang, W. Zhu, A. Casimir, H. Zhu, A. Mendoza-Garcia and S. Sun, *Nano Lett.*, 2015, **15**, 2468–2473.
26 D. L. Wang, H. L. L. Xin, R. Hovden, H. S. Wang, Y. C. Yu, D. A. Muller, F. J. DiSalvo and H. D. Abruna, *Nat. Mater.*, 2013, **12**, 81–87.
27 W. Xiao, W. Lei, M. Gong, H. L. Xin and D. Wang, *ACS Catal.*, 2018, **8**, 3237–3256.
28 Y. Liu, M. Wei, D. Raciti, Y. Wang, P. Hu, J. H. Park, M. Barclay and C. Wang, *ACS Catal.*, 2018, **8**, 10931–10937.
29 W. Gao, X. Y. Li, Y. H. Li, X. Wang, S. Y. Song and H. J. Zhang, *CrystEngComm*, 2012, **14**, 7137–7139.
30 Y. Liu, D. Li, V. R. Stamenkovic, S. Soled, J. D. Henao and S. Sun, *ACS Catal.*, 2011, **1**, 1719–1723.
31 X. Lu, Z. Deng, C. Guo, W. Wang, S. Wei, S. P. Ng, X. Chen, N. Ding, W. Guo and C. M. Wu, *ACS Appl. Mater. Interfaces*, 2016, **8**, 12194–12204.
32 A. L. Wang, C. L. Liang, X. F. Lu, Y. X. Tong and G. R. Li, *J. Mater. Chem. A*, 2016, **4**, 1923–1930.
33 J. Xie, Q. Zhang, L. Gu, S. Xu, P. Wang, J. Liu, Y. Ding, Y. F. Yao, C. Nan, M. Zhao, Y. You and Z. Zou, *Nano Energy*, 2016, **21**, 247–257.
34 H. J. Huang, J. X. Zhu, D. B. Li, C. Shen, M. M. Li, X. Zhang, Q. G. Jiang, J. F. Zhang and Y. P. Wu, *J. Mater. Chem. A*, 2017, **5**, 4560–4567.
35 H. Huang, Y. Liu, Q. Gao, W. Ruan, X. Lin and X. Li, *ACS Appl. Mater. Interfaces*, 2014, **6**, 10258–10264.

36 Z. Zhang, Q. Wu, K. Mao, Y. Chen, L. Du, Y. Bu, O. Zhuo, L. Yang, X. Wang and Z. Hu, *ACS Catal.*, 2018, **8**, 8477–8483.
37 Y. Qu, Y. Gao, L. Wang, J. Rao and G. Yin, *Chemistry*, 2016, **22**, 193–198.
38 J. Wang, M. Xu, J. Zhao, H. Fang, Q. Huang, W. Xiao, T. Li and D. Wang, *Appl. Catal., B*, 2018, **237**, 228–236.
39 J. Zhu, X. Zheng, J. Wang, Z. Wu, L. Han, R. Lin, H. L. Xin and D. Wang, *J. Mater. Chem. A*, 2015, **3**, 22129–22135.
40 J. Shim, J. Lee, Y. Ye, J. Hwang, S. K. Kim, T. H. Lim, U. Wiesner and J. Lee, *ACS Nano*, 2012, **6**, 6870–6881.
41 J. T. L. Gamler, H. M. Ashberry, S. E. Skrabalak and K. M. Koczkur, *Adv. Mater.*, 2018, e1801563, DOI: 10.1002/adma.201801563.
42 R. Rizo, D. Sebastian, M. J. Lazaro and E. Pastor, *Appl. Catal., B*, 2017, **200**, 246–254.
43 Y. Bao, F. Wang, X. Gu and L. Feng, *Nanoscale*, 2019, **11**, 18866–18873.
44 M. Roca-Ayats, O. Guillén-Villafuerte, G. García, M. Soler-Vicedo, E. Pastor and M. V. Martínez-Huerta, *Appl. Catal., B*, 2018, **237**, 382–391.

 